CONF-9606108--2

Fermi National Accelerator Laboratory

Physics with the DØ Calorimeter

. J. Kotcher
Representing the DØ Collaboration

Brookhaven National Laboratory
Upton, New York 11973

Fermi National Accelerator Laboratory
P.O. Box 500, Batavia, Illinois 60510

RECEIVED
SEP 23 1996
OSTI

August 1996

MASTER

Disclaimer

DISCLAIMER

Portions of this document may be illegible
in electronic image products. Images are
produced from the best available original
document.

PHYSICS WITH THE DØ CALORIMETER

Jonathan Kotcher
(representing the DØ Collaboration)
Brookhaven National Laboratory
Upton, New York 11973, USA

ABSTRACT

The DØ detector, located at the Fermi National Accelerator Laboratory in Batavia, Illinois, USA, is a large hermetic detector designed to study the products of $\bar{p}p$ collisions at a center-of-mass energy of $\sqrt{s} = 1.8$ TeV. The centerpiece of the detector is uranium/liquid argon sampling calorimetry, which provides high resolution detection of the physics signatures of interest – electrons, photons, jets, and missing transverse energy – over the full solid angle. We discuss below how the calorimeter information is used to detect the final states relevant to the physics we are pursuing, and describe a number of physics processes and results that demonstrate the utility of some of our design choices.

1 Introduction

The DØ detector, located at the Fermi National Accelerator Laboratory, is a large multi-purpose detector designed for the study of high mass and large transverse energy (E_T) phenomena in high energy proton-antiproton collisions. The detector stresses coverage over a large solid angle for electrons, muons, and jets, with the presence of neutrinos inferred from the measurement of missing E_T ($\not{E}_T$). The heart of the device is hermetic uranium/liquid argon sampling calorimetry, designed to provide homogeneous, high-precision energy measurements of electrons and jets over a large range in pseudorapidity. [1] The calorimeter is complemented by a series of inner tracking chambers that provide charged particle tracking and vertex identification, and an outer 4π muon system, for identification and momentum measurement of muons.

The physics program being pursued by DØ includes studies of the top quark, jet physics (including tests of quantum chromodynamics and composite-ness searches), studies of the intermediate vector bosons (such as the W mass and width, vector boson self-couplings, and W/Z production in association with jets), and searches for evidence of new and exotic phenomena, including supersymmetry, fourth generation quarks, and heavy vector bosons. We have collected a total integrated luminosity of 120 pb^{-1} during the last Tevatron running cycle, which took place from May, 1992 through February, 1996.

This paper describes how the calorimeter information is integrated into the physics analyses of interest at DØ, using specific physics channels to demonstrate the methods used. It has been organized around the means of determining (or identifying) the four basic event signatures of most interest from a calorimetric standpoint: electrons, photons, jets, and $\not{E}_T$. Physics results best illustrating the design features and identification strategies in each of the categories are presented.

2 The DØ Detector

The innermost detector subsystem at DØ is the tracking system, which consists of three subsystems. Immediately surrounding the beampipe is the vertex chamber, designed for the reconstruction of primary and secondary vertices. This is followed by a transition radiation detector (TRD), employed to enhance electron identification by rejecting charged pions and photon conversions. The outermost tracking detectors consist of a central and forward/backward drift chambers, which provide charged-particle tracking and dE/dx information to $|\eta| \approx 3.2$. The calorimeters surround the tracking volume.

The muon system, consisting of five magnetized toroids together with sets of proportional drift chambers, provides momentum measurements and additional tracking information for muons to $|\eta| \approx 3.3$.

2.1 A Few Details on the Calorimeter

The calorimeters are housed in three separate cryostats: a central calorimeter (CC), and two end calorimeters (EC's). The active volume is segmented into modular structures consisting of three distinct regions: the electromagnetic (EM), fine hadronic (FH), and coarse hadronic (CH) sections. The EM and FH regions employ uranium absorber; the coarse sections, which sample the tail-end of hadronic showers, consist of either copper or steel absorber. The electromagnetic (hadronic) coverage of the calorimeter extends to $|\eta| \approx 4.1$ (5.2).

The readout is arranged into $\approx$ 5,000 semi-projective towers of size 0.1×0.1

in $\Delta\eta \times \Delta\phi$. In order to enhance the position resolution for electrons and photons, the transverse readout segmentation at electromagnetic shower maximum (EM readout layer 3) is twice as fine in each dimension (0.05×0.05). The EM section is read out four times – after 2, 2, 7, and 10 radiation lengths (X_0) – which provides information on the longitudinal development of the shower. The hadronic section is read out one to four times, depending on the η-region.

A minimum ionizing particle (mip) liberates $\approx 20,000$ electrons in a liquid argon gap, which corresponds to about 3 femtocoulombs of charge, or ≈ 4 ADC counts in our unit of readout. A least count in the calorimeter is therefore equal to approximately 5,000 electrons, or 1/4 of an equivalent mip signal. The full dynamic range of the electronics is 15 bits, or $\approx 32,000$ ADC counts. The calorimeter readout can accommodate incident electrons with energies of up to ≈ 400 GeV before any saturation effects become relevant.

The total thickness of the calorimeter varies from ≈ 7 to 9 interaction lengths (λ_0), depending on pseudorapidity. In addition to improving the jet resolution by containing hadronic showers, the large amount of material helps to limit hadronic punch-through to the outer muon system. The EM section is a total of 21 X_0 deep.

In order to improve the energy resolution for particles that traverse the inter-cryostat region (ICR), which covers the region $0.8 < |\eta| < 1.4$, both "massless gaps" and an inter-cryostat detector (ICD) have been added. The "massless gaps", so named because they contain no absorber material, are located between the modules and the cryostat in the liquid. They sample the shower energy that is lost by particles that traverse the module endplates and cryostat walls. The ICD, located between the cryostats in the η-region defined above, consists of scintillator tiles that play a similar role.

The reader is directed to Refs. [2, 3] for further details on the overall detector, including the calorimeter.

3 Electron Identification

Electron identification at DØ relies predominantly on the calorimeter information, with complementary measurements provided by the tracking chambers. A brief description of the process is presented below.

Electron candidates are identified in the offline reconstruction by forming nearest neighbor clusters of electromagnetic (EM) readout towers. A series of selection criteria are then imposed:

- *Cluster (shower) shape:* The shower shape of the candidate cluster is re-

quired to be consistent with that of an electron. The determination employs a covariance-matrix technique, [4] in which 41 observables are used to determine the probability that a given electromagnetic cluster resulted from energy deposited by an electron (or photon). The variables used include the fractional energies in EM layers 1, 2 and 4, and the fractional energies in a 6×6 array in the more finely segmented EM layer 3, thereby exploiting both the transverse and longitudinal readout segmentation of the calorimeter. The covariance matrix is "trained" on Monte Carlo data at various energies, which has in turn been developed from test beam information.

- *Longitudinal isolation:* The amount of cluster energy contained within the EM portion of the calorimeter is required to exceed (typically) $\approx 90\%$ of the cluster energy in the four EM layers plus the first fine hadronic layer.

- *Transverse isolation:* The isolation fraction, f_{iso}, defined by:

$$f_{iso} = \frac{\text{E}(R < 0.4) - \text{EM}(R < 0.2)}{\text{EM}(R < 0.2)}, \tag{1}$$

is required to be (typically) less than 10%. Here, E (EM) is the total (electromagnetic) energy contained within a cone of radius R centered on the candidate cluster, where $R = \sqrt{(\Delta\eta)^2 + (\Delta\phi)^2}$.

- *Track match:* A suitable spatial match between the calorimeter cluster and a reconstructed drift chamber track is required. The track match significance, σ_{track}, is the figure of merit used:

$$\sigma_{track} = \sqrt{\left(\frac{\Delta\phi}{\delta_{\Delta\phi}}\right)^2 + \left(\frac{\Delta z(r)}{\delta_{\Delta z(r)}}\right)^2}, \tag{2}$$

where the variable Δz (Δr) is used in CC (EC). The quantity δ_x is the resolution in the variable x.

- *Track ionization:* In order to reject photons that convert upstream of the calorimeter, the dE/dx energy loss as measured in the drift chambers is required to be consistent with that of an electron (*i.e.*, 1 mip vs. 2 mip tracks).

- *TRD energy deposition:* The energy deposited in the TRD is used to reject charged pion backgrounds and photon conversions.

The last two items are used optionally, depending on the demands of particular analyses. In general, cuts on the above variables are most frequently applied independently; they can, however, be applied collectively through a likelihood technique which has recently been developed. [5]

3.1 Absolute Energy Scale

The electromagnetic energy scale, which anchors all of the energy measurements in the experiment, is determined by calibrating to the $Z \rightarrow ee$ resonance. The energies of all identified EM objects in physics analyses – i.e., identified electrons and photons – are scaled by the ratio of the Z mass as measured at LEP [6] to that measured at D∅ (i.e., $M_Z^{LEP}/M_Z^{D\emptyset}$). Test beam studies have demonstrated the calorimeter to be linear to better than $\approx 0.5\%$ for electron energies greater than 10 GeV, implying that, for electrons at or above this p_T, any intrinsic non-linearity of the detector makes a negligible contribution to the error incurred from this scaling procedure.[1]

Prior to the final assembly of the entire detector, one of the two end calorimeter EM modules, and four prototype EM modules from the central calorimeter, were tested in independent beam tests at the Fermilab fixed target facility. [7] A series of calibration constants, such as layer-to-layer sampling weights, as well as overall ADC-to-GeV conversion factors, were carried over to the main experiment for each cryostat "type" independently. In addition, the liquid argon purity and temperature (and therefore the response) can vary from cryostat to cryostat. Considerations of this kind have motivated our decision to establish the Z mass, and hence the scale factor, in each of the cryostats independently.
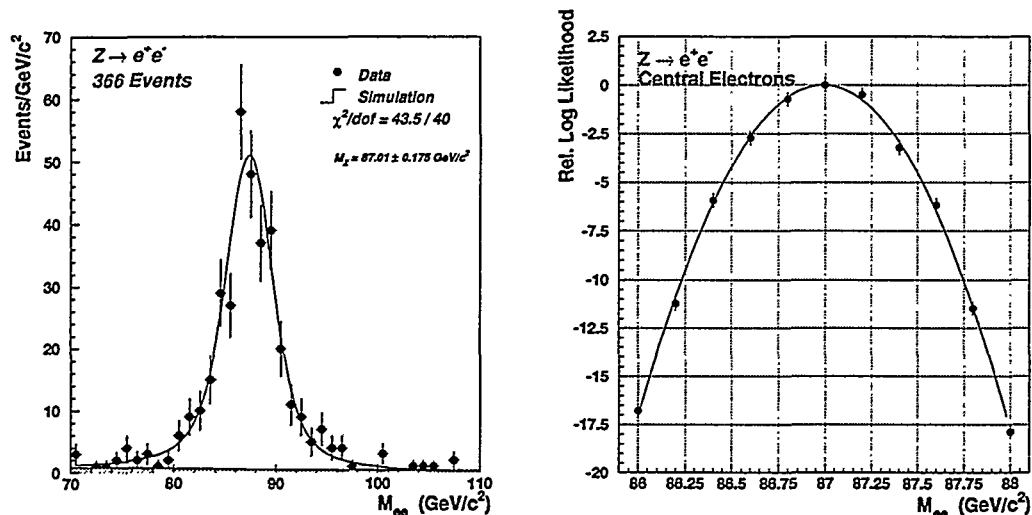

Figure 1: Dielectron mass distribution, with background estimation (shaded area) and fitting results, for events where both electrons are central ($|\eta| < 1.0$) (left). The relative log likelihood as a function of mass (right). The spectra are based on the analysis of 12.8 pb^{-1} of data.

Our reconstructed dielectron mass distribution for central electrons is shown in Fig. 1. The spectrum is fit to a relativistic Breit-Wigner line shape, convoluted

---

[1]This assumes that the portion of the deviation of $M_Z^{LEP}/M_Z^{D\emptyset}$ from unity that might be due to an offset, rather than a pure scale factor, is negligibly small. (see Section 3.1.1)

with a Gaussian to simulate detector noise and resolutions. The relative log likelihood resulting from these fits are shown as well.

For most of the physics of interest at DØ, the accuracy of the above procedure is sufficient. An example of a measurement where a more precise determination of the energy scale is needed is the precision measurement of the mass of the W boson. [8] We discuss below our means of establishing the error associated with the energy scale in this measurement.

3.1.1 Energy Scale Error in the Determination of the W Mass

The W mass, which is measured from $W \rightarrow e\nu$ decays at DØ, is in practice extracted from the W to Z mass ratio, i.e. $M_W = (M_W^{D\emptyset}/M_Z^{D\emptyset}) \times M_Z^{LEP}$. A number of systematic effects common to the two measurements cancel in this ratio. Most relevant to this discussion is that, to first order, the ratio is insensitive to the electromagnetic energy scale. To establish the scale error with the precision required here, it is important to quantify the extent to which a potential offset – as opposed to a scale factor – is responsible for the deviation of the ratio $M_Z^{LEP}/M_Z^{D\emptyset}$ from unity. We use reconstructed low energy resonances, in conjunction with the information extracted from the $Z \rightarrow ee$ resonance, to establish the energy scale with the necessary precision.
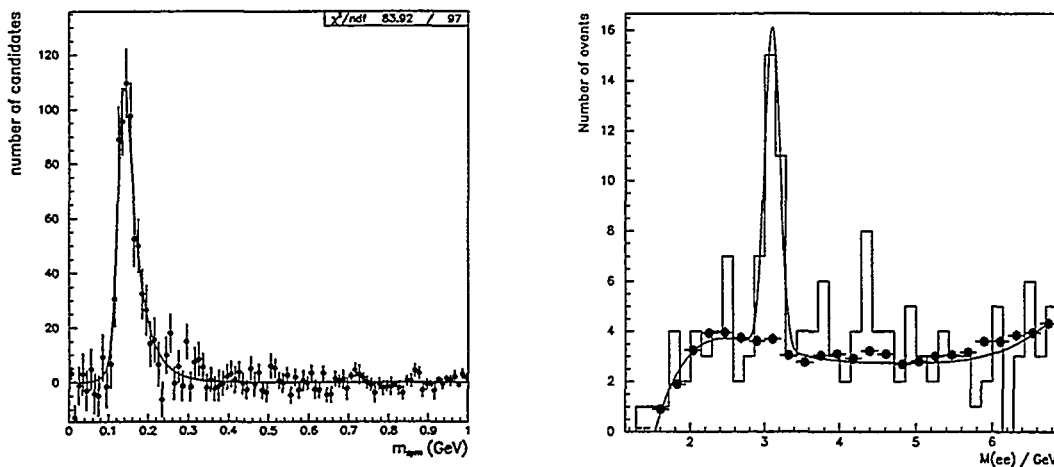

Figure 2: Background-subtracted $\pi^0 \rightarrow \gamma\gamma \rightarrow eeee$ peak, with fit. We measure $m_{\pi^0} = 134.5 \pm 10.2$ MeV/c^2 (left). Low-E_T ($E_T^e < 3$ GeV/c) dielectron invariant mass, showing the J/ψ peak and a fit to the distribution (including background). The measured J/ψ mass is $m_{J/\psi} = 3.032 \pm 0.193$ GeV/c^2 (right). (Errors quoted represent both the statistical and systematic contributions added in quadrature.)
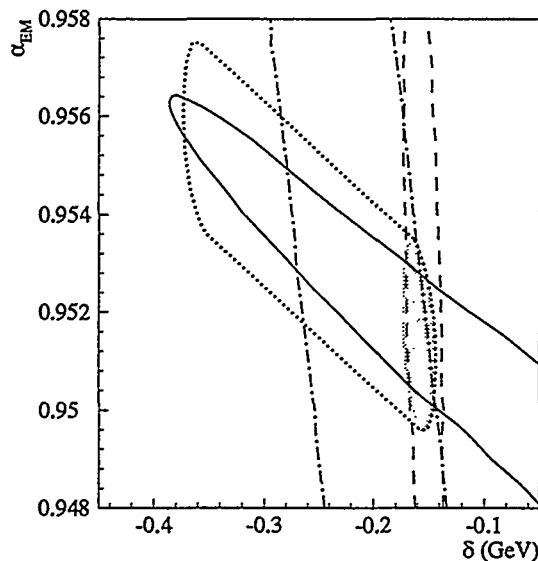
Figure 3: Constraints on the scale factor α and intercept δ from observed $J/\psi \rightarrow ee$ (dashed-dotted line), $\pi^0 \rightarrow \gamma\gamma$ (dashed line), and $Z \rightarrow ee$ decays (solid line). The shaded inner contour shows the combined result. The dotted line indicates the allowed area when nonlinear terms, constrained from test beam measurements, are included.

We assume that the measured and true calorimeter energies are related to one another through the relation $E_{meas} = \alpha E_{true} + \delta$, where α and δ are the energy scale factor and offset, respectively. Forming the invariant mass of a two-pronged decay with the above assumed functional form, and keeping terms to first order in δ, results in an expression for the invariant mass that is given by $m_{meas} = \alpha m_{true} + \delta f$. The variable $f = \frac{2(E^1_{meas} + E^2_{meas})}{m_{meas}} \sin^2(\omega/2)$, and is determined purely from the kinematics of the decay. The quantity ω is the opening angle between the two electrons. The scale error on the W mass is determined by the value of, and the error on, α and δ, and the correlations between them.

We use reconstructed $\pi^0 \rightarrow \gamma\gamma$ decays, where both photons convert, and $J/\psi \rightarrow ee$ decays, in conjunction with the information from the Z, to evaluate the offset and scale factor *in situ*. The reconstructed π^0 and J/ψ peaks are shown in Fig. 2. These resonances decay to electrons or photons with energies that are, on average, below 10 GeV, compared with the $\approx$ 40 GeV electrons from Z decay. Each of the resonances therefore has a different sensitivity to α and δ and, taken together, provide a powerful tool for establishing the electromagnetic scale *in situ*.

The one-sigma contours in α and δ for the three resonances, obtained from the data in conjunction with Monte Carlo simulations, are shown in Fig. 3. We obtain a value for the energy scale factor $\alpha = 0.9514 \pm 0.0018^{+0.0061}_{-0.0017}$ and the offset

$\delta = (-0.158 \pm 0.015^{+0.03}_{-0.21})$ GeV. The asymmetric errors are due to possible response nonlinearities for low energy electrons, which we constrain from test beam data. From these data, we obtain a scale error on the W mass of 80 MeV/c^2 from the analysis of 76 pb^{-1} of data. This represents roughly half of the total error in the measurement, which is currently 170 MeV/c^2.

The influence of the large relative systematic error on δ on the energy scale error is suppressed (to first order) in the W-to-Z mass ratio. At this point, we find that the scale error on the W mass is dominated by the statistics of the Z.

3.2 Low p_T electrons

The importance of being able to detect electrons at low p_T and over a broad range in pseudorapidity is well illustrated in gaugino ($\tilde{W}_1 \tilde{Z}_2$) searches, where we select final states consisting of three leptons and $\not{E}_T$. The signature of interest here is those in which the W and Z, produced in association with two non-interacting $\tilde{Z}_1$'s, both decay leptonically to final states consisting of eee, $ee\mu$, $e\mu\mu$, or $\mu\mu\mu$, along with a neutrino (or anti-neutrino). The backgrounds for this process are small; observation of a measurable signal in this distinctive SUSY channel would be quite compelling. The expected cross section times the branching ratio ($\sigma \cdot B$) for these processes, however, are also quite small, underscoring the utility of increased acceptance in this measurement.

The leptons carrying the least amount of transverse energy in these decays tend to be soft, with a large fraction of them produced in the forward direction. In the eee channel, a $\tilde{W}_1$ mass of 45 (100) GeV is expected to result in a final state in which 90 (50)% of the softest electrons (i.e., the third leading electrons) have p_T below 10 GeV, with roughly 30 (25)% of these produced in the pseudorapidity range $1.5 < |\eta| < 2.5$. [2]

The overall analysis efficiency for the eee channel – which is the product of the efficiencies due to the geometric and kinematic acceptance, offline selection cuts, and the trigger – has been determined to be 2.4 (15.6)% for the lower (higher) $\tilde{W}_1$ masses quoted above. The low efficiency is, in part, an indication of the difficulty of doing physics with electrons (and muons) that are produced over a broad range in pseudorapidity, with a significant fraction of them at low p_T. We have nevertheless been able to exclude regions of the relevant parameter space via this distinctive channel, in part because of our forward calorimetry (see Fig. 4). [9]

---

[2]The range $1.5 < |\eta| < 2.5$ is the region where, in practice, the forward electromagnetic calorimeter is sensitive. EM coverage in the central region extends to $|\eta| < 1.1$; the region $1.2 < |\eta| < 1.4$ lacks any EM coverage.
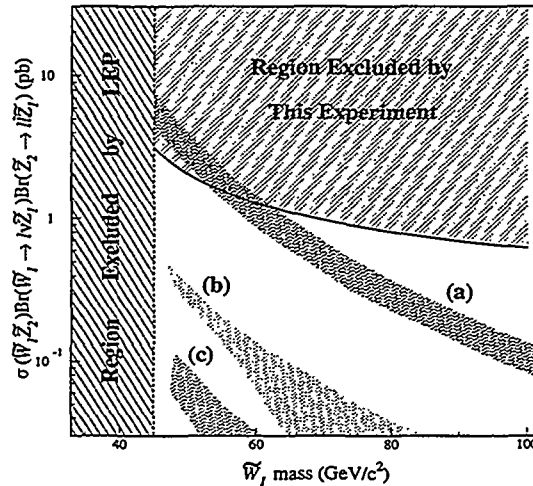
Figure 4: The 95% confidence limit on cross section times branching ratio into eee, $ee\mu$, $e\mu\mu$, or $\mu\mu\mu$, as a function of $M_{\tilde{W}_1}$, along with the region of $M_{\tilde{W}_1}$ excluded by LEP. The bands represent the expected limits for different treatments of the theory.

4 Photon Identification

There are a number of physics signatures of interest at the Tevatron containing final state photons that make photon detection an important design consideration. A partial list includes the single (direct) photon cross section, the diphoton cross section and mass distribution, measurement of the intrinsic transverse momentum of the incoming partons (k_T) in diphoton final states, and γ/jet angular distributions. In addition, the $W\gamma$ and $Z\gamma$ diboson couplings are explored via their rather distinctive $e/\mu/\gamma$ final states.

The techniques and criteria applied for photon identification at DØ are analogous to those for electron identification, except that there is required to be no track pointing to the electromagnetic cluster. Similar cuts related to cluster shape and isolation, and electromagnetic energy fraction, are applied.

4.1 Direct Photon Cross Section

The primary experimental challenge in the measurement of the inclusive photon cross section is the extraction of the prompt photon signal from the copious backgrounds due to π^0 and η meson decays to photons. We use the calorimetric quantity $\log(\text{EM1}/E_{tot})$ to determine the photon purity (or background fraction), where EM1 is the energy deposited in the first electromagnetic layer, and E_{tot} is the total energy of the cluster. The dominant background consists of boosted diphotons from meson decay (*i.e.*, π^0 or $\eta \to \gamma\gamma$). Over most of the p_T regime of interest, the transverse segmentation of the calorimeter is too coarse to spatially resolve the photon pair

into its two components. Instead, we exploit the longitudinal readout segmentation: the meson decay backgrounds, consisting as they do of two photons, are twice as likely to convert in the first EM layer than a single photon, and will therefore shower earlier. The background is therefore expected to deposit more energy in the initial layer of the calorimeter than the single, prompt photon.

The central and forward photon cross sections, [10] spanning a photon p_T range of ≈ 10 to 100 GeV, are shown in Fig. 5. The dotted line represents a next-to-leading order (NLO) theoretical calculation by Baer, Ohnemus, and Owens, [11] in which CTEQ2M [12] parton distribution functions have been used. The cross section in the range $1.6 < |\eta| < 2.5$ is a new one at hadron colliders. The primary strength of DØ's contribution to physics involving photons arises from this increase in acceptance. The additional acceptance has also measurably improved our physics capability in exploring the diboson couplings. [13]
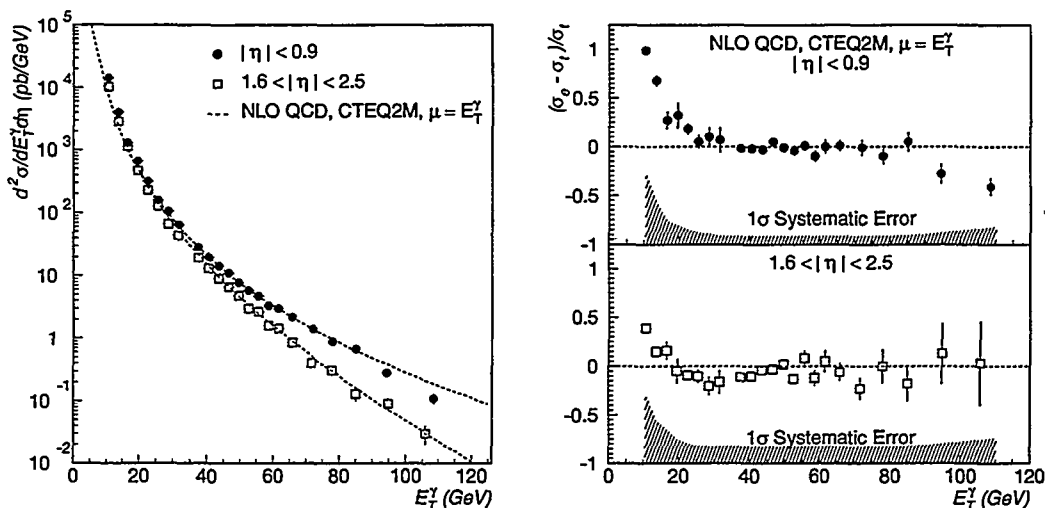

Figure 5: Direct photon cross section for the central ($|\eta| < 0.9$) and forward ($1.6 < |\eta| < 2.5$) regions, along with a theoretical calculation (left). $(\sigma_{exp} - \sigma_{theory})/\sigma_{exp}$ taken from previous plot, including the 1-σ systematic error band (right). (*DØ Preliminary*)

5 Jets

There are three basic jet-finding algorithms being employed at DØ. For the physics we have reported on to date, the fixed cone algorithm is most commonly in use. Cone sizes ΔR of 0.3, 0.5 and 0.7 are employed by default in the event reconstruction, where $\Delta R = \sqrt{(\Delta\phi)^2 + (\Delta\eta)^2}$. A nearest neighbor clustering algorithm, similar in concept to that used in our electron finding, and a k_T algorithm, are also being pursued. In the interests of space, we discuss only the cone algorithm below.

In the fixed cone algorithm, the hadronic and electromagnetic E_T in towers of size 0.1×0.1 in $\Delta\eta \times \Delta\phi$ is summed. All towers with $E_T > 1$ GeV are considered "seed" towers, and jets are constructed about these towers within a cone size of a given ΔR. The jet direction, defined in terms of the measured jet energy and its x, y, and z components, is computed, and the process is repeated using the new jet direction as the jet center. The above is iterated until the jet direction is stable. Only jets with $E_T > 8$ GeV are kept in the final jet list for use in offline analyses. The reader is referred to Ref. [14] for more detailed information on the cone algorithm used at DØ.

Our jet calibration [15] consists of a series of steps that correct the raw measured jet energy (or E_T) for a number of effects, including zero suppression of our asymmetric pedestals, underlying energy from the spectator interaction, particle showering outside of the jet cone, and response variations correlated with jet width. The overall hadronic scale is derived from balancing the $\not{E}_T$ in photon-jet events. The minimization of dead regions and cracks in the calorimeter, the demonstrated linearity of the device, and the uniform technology have helped control the magnitude of the jet corrections that we need to apply: for central ($|\eta| < 0.5$) jets, for example, we never correct jet energies by more than 20% for jets of any accessible p_T value.

5.1 Jet Physics Topics

Full coverage, as well as effective control of all sources of noise (coherent and incoherent), are design features that directly impact studies of rapidity gaps between jets. We use the measurement of the energy flow between jets produced at large $|\eta|$ to distinguish between $\bar{p}p$ processes resulting from color singlet exchange, and those resulting from exchange of a color octet (i.e., a gluon). [16] Dijet events with both jets having $|\eta| > 2$ are chosen, and are classified according to the sign of the product $\eta_1 \cdot \eta_2 \equiv \beta$. Events with a positive (negative) value of β contain two jets produced on the same (opposite) side(s) of the calorimeter.

Opposite-side events are expected to contain a significant component due to color singlet exchange. This component is discernible as an excess of events with little or no associated activity in the central region. The same-side events are expected to be dominated by color octet exchange, and are used as a control. These events should result in a smooth distribution of centrally-produced particles. In either case, the energy distribution of the particles produced in the central ("non-jet") region is expected to be soft, implying that high resolution, low-noise calorimetry is a particularly desirable feature here.

The number of calorimeter towers above threshold (n_{cal}) versus the number
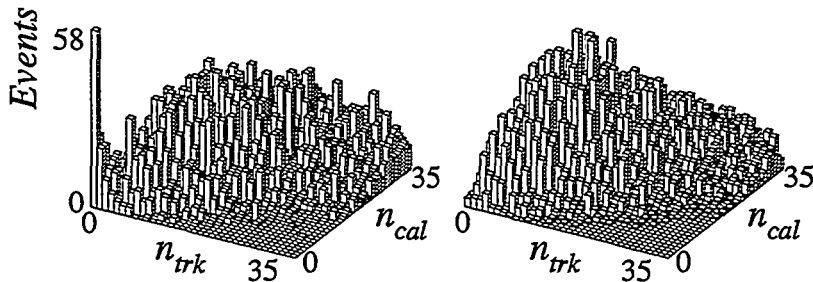
Figure 6: Number of calorimeter towers above threshold (n_{cal}) versus number of reconstructed central drift chamber tracks (n_{trk}) for $|\eta| < 1.3$ in opposite-side (left) and same-side (right) events. The excess at low track multiplicity/low number of towers above threshold is interpreted as evidence of color singlet exchange.

of tracks reconstructed in the central region (n_{trk}) is shown for the two samples in Fig. 6. The excess of opposite-side events that have small values for both n_{trk} and n_{cal} are clearly visible. The calorimeter threshold used in the analysis is 200 (400) MeV for EM (hadronic) towers, which effectively eliminates most towers containing only noise. Typical noise levels of 30 (100) MeV in an EM (hadronic) tower, and average energy deposition for minimum ionizing particles of ≈ 300 (1000) MeV per tower, have been measured *in situ*. Our ability to resolve small signals over noise is quite useful in analyses of this kind. From these data, we measure a fractional excess of color singlet above color octet exchange of 1.07 ± 0.10 (stat) $^{+0.25}_{-0.13}$ (syst)%.

The processes involved in rapidity gap physics help to demonstrate the importance of calorimetry that is stable and well-characterized at the low end of the dynamic range. At the other end of the scale (*i.e.*, high-E_T), shower containment is an important consideration, as it helps to mitigate the effects of fluctuations in unseen energy that can escape the calorimeter in the longitudinal direction. Broad dynamic range of the calorimeter readout is also desirable, as one would like to avoid any saturation effects that might induce biases, particularly as a function of E_T. In the central (forward) inclusive jet cross section, for example, jet energies of up to ≈ 450 (600) GeV are probed. Shape variations in the inclusive jet cross section can be a signature of new physics; minimization of these types of potentially E_T-dependent biases is therefore an important concern.

Our measurement of the inclusive jet cross section for $|\eta| < 0.5$ is shown in Fig. 7. Also shown is comparison of the data with a NLO theoretical calculation [17] that uses as input a few different CTEQ parton distribution functions. The cross section falls by some seven decades over the ≈ 450 GeV E_T interval. It is clear from the data that the theoretically predicted shape of the distribution is quite sensitive to the chosen set of parton distribution functions. The jet energy scale uncertainty

is the dominant source of systematic error, contributing up to 30% to the systematic error at high-E_T. Efforts are underway to reduce the error in the jet energy scale, as well as the overall systematic uncertainty in the cross section.
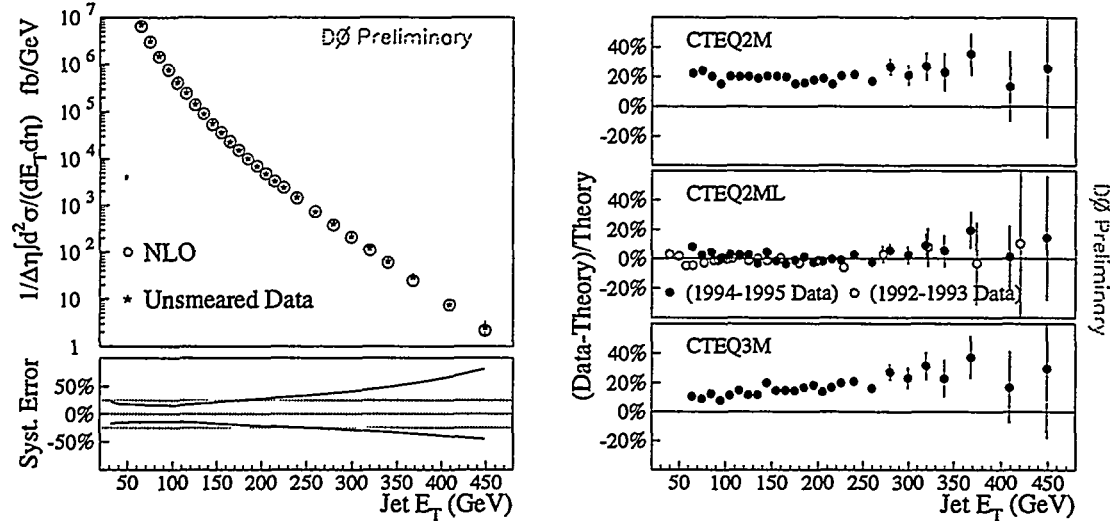

Figure 7: The central inclusive jet cross section, with a comparison to next-to-leading order theory. The systematic error band is shown below (left). Comparison of the data with a few different parton distribution functions. A comparison of early and late data sets are shown in the middle plot (right). (Errors in series of plots on right hand side are statistical only.) (*DØ Preliminary*)

Exploiting the physics that forward $|\eta|$ coverage can provide – particularly in jet physics – constitutes a major portion of the physics program at DØ. We direct the reader to Refs. [14, 18, 19, 20] for a description of a few of these topics.

6   Missing E_T ($\not{E}_T$)

Homogeneity of response and good resolution is also advantageous in the determination of $\not{E}_T$, which is defined as follows:

$$\vec{\not{E}}_T = - \sum_{i=1}^{N_{cells}} \vec{E}_{T_i}. \tag{3}$$

The sum is over all cells in the calorimeter. This quantity is optionally corrected for energy detected in the inter-cryostat region, or the measured momentum of muons in the event, or both.

Inclusion of the ICR energy has been shown to significantly enhance the resolution in $\not{E}_T$. We use QCD multi-jet events, where any measured $\not{E}_T$ results primarily from instrumental effects, to quantify this effect (there should be little or no physics-related $\not{E}_T$ in these events). Computing the $\not{E}_T$ both with and without

ICR corrections in the same set of multi-jet events, we find a $\approx 44\%$ reduction in the number of events with $\not{E}_T > 30$ GeV after ICR corrections are applied. Cryogenic systems, which unavoidably introduce (usually sizable) inter-cryostat boundaries, invariably suffer from incomplete sampling in these regions. Global event variables, such as $\not{E}_T$, can be particularly sensitive to such dead spaces. The above number gives a semi-quantitative indication of how important recovering the energy in these detector regions can be.

Missing E_T is of course of great utility in high-p_T physics, particularly that involving final state W bosons that decay leptonically to a charged lepton and a ("invisible") neutrino. Top pair production, in which both top quarks decay to a W and a b quark, as well as a variety of electroweak topics involving W production, exploit $\not{E}_T$ in the detection of the relevant final states. $\not{E}_T$ is also particularly useful in SUSY and new phenomena searches, which are often expected to result in non-interacting final state particles, such as neutralinos or neutrinos.

The exclusion contour resulting from our squark–gluino search is shown in Fig. 8. The data for this analysis was acquired with a software trigger consisting only of a $\not{E}_T$ requirement, with a threshold that varied from 20 or 40 GeV during the run. The additional region of the parameter space that has been eliminated since our recent PRL publication [21] has resulted from a parallel ("updated") analysis in which the offline $\not{E}_T$ cut was reduced from 75 to 65 GeV, and an additional jet was required. The lower $\not{E}_T$ cut is helpful only because the variable is well-behaved – even at reasonably small values – and because fake $\not{E}_T$, which is dominated by instrumental effects and dead regions, is at some level corrected for in the DØ design.

7 Conclusion

Calorimetry, which is the heart of the DØ detector, is critical to the physics being pursued by the collaboration. The fine segmentation and superior energy resolution offer good electron and photon identification over the full solid angle, important for the broad variety of physics topics involving W and Z bosons, as well as final state photons. The uniformity of the response and technology, coupled with the full coverage, enhances many of the opportunities in jet physics, where the full shower containment, low noise, and broad dynamic range enhance the physics reach. The calorimetric energy resolution and hermeticity offer stable, high-resolution measurements of $\not{E}_T$, useful in a variety of physics processes.

With the addition of a central and forward preshower system, an improved inner tracking system (including a silicon vertex chamber and scintillating fiber tracker), and a central magnetic field, the upgraded DØ detector has been designed
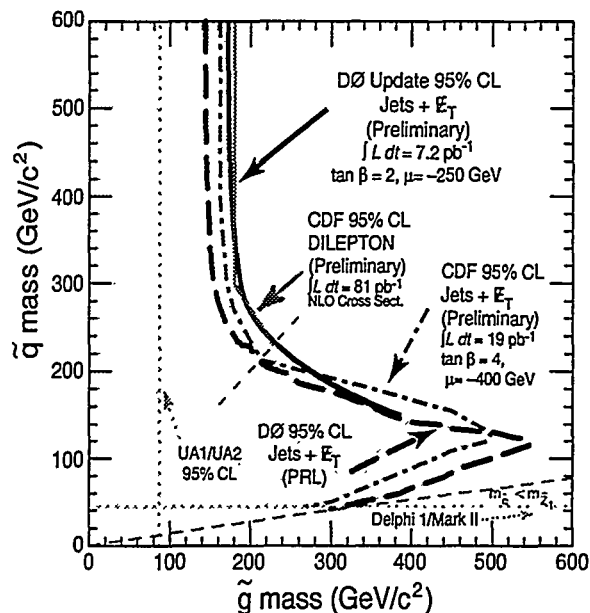
Figure 8: Squark-gluino exclusion contour.

with an eye toward continuing to exploit the detector's already-existing calorimetric strengths. We look forward to continuing our pursuit of a broad physics program during the coming Main Injector era at the Tevatron.

References

1. The pseudorapidity, η, is defined by the relation $\eta \equiv -\ln[\tan(\theta/2)]$, where θ is the polar angle with respect to the proton-beam direction. The z axis in the D∅ coordinate system is along the beam axis, r is the distance perpendicular to that axis, and ϕ is the polar angle.

2. S. Abachi et al., Nucl. Instr. Meth. A338, 185 (1994).

3. J. Kotcher, "Design, Performance, and Upgrade of the D∅ Calorimeter", Proceedings of the 1994 Beijing Calorimetry Symposium, IHEP - Chinese Academy of Sciences, Beijing, China, October 25-27, 1994, pp. 144-158; J. Kotcher, "Upgrade Plans for the D∅ Calorimeter", these proceedings.

4. S. Abachi et al., Phys. Rev. D52, 4877 (1995).

5. M. Narain and U. Heintz, "A Likelihood Test for Electron ID", D∅ Internal Note #2386 (December, 1994).

6. The value for the Z mass we use is $M_Z^{LEP} = 91.1884 \pm 0.0022$ GeV/c^2, from P. Renton, "Precision Tests of the Electroweak Theories", Lepton-Photon Con-

ference, Beijing, P.R. China (1995), OUNP-95-20. For reference, we quote the world value of the π^0 and J/ψ masses: $m_{\pi^0} = 0.1350 \pm 0.0006$ GeV/c^2 and $m_{J/\psi} = 3.09688 \pm 4 \times 10^{-5}$ GeV/c^2, from Particle Data Group, L. Montanet *et al.*, *Phys. Rev.* **D50**, 1173 (1994).

7. H. Aihara *et al.*, *Nucl. Instr. Meth.* **A325**, 393 (1993).

8. S. Abachi *et al.*, FERMILAB-PUB-96/177-E, submitted to *Phys. Rev. Lett.*

9. S. Abachi *et al.*, *Phys. Rev. Lett.* **76**, 2228 (1996).

10. S. Abachi *et al.*, FERMILAB-PUB-96/072-E, submitted to *Phys. Rev. Lett.*

11. H. Baer, J. Ohnemus, and J.F.Owens, *Phys. Rev.* **D42**, 61 (1990).

12. CTEQ Collaboration, J. Botts *et al.*, *Phys. Lett.* **B304**, 159 (1993).

13. S. Abachi *et al.*, *Phys. Rev. Lett.* **75**, 1028 (1995); S. Abachi *et al.*, *Phys. Rev. Lett.* **75**, 1034 (1995); S. Abachi *et al.*, FERMILAB-PUB-96/115-E, submitted to *Phys. Rev. Lett.*

14. H. Weerts, "Studies of Jet Production with the DØ Detector", *Proceedings of the 9th Topical Workshop on Proton–Antiproton Collider Physics*, University of Tsukuba, Ibaraki, Japan, October 18-22, 1993, p. 192; N. Hadley, "Cone Algorithm for Jet Finding", DØ Internal Note #904 (November, 1989).

15. B. Kehoe, "Hadronic Calibration of the DØ Calorimetry", these proceedings.

16. S. Abachi *et al.*, *Phys. Rev. Lett.* **76**, 734 (1996).

17. S.D. Ellis, Z. Kunszt, and D.E. Soper, *Phys. Rev. Lett.* **64**, 2121 (1990); F. Aversa *et al.*, *Phys. Rev. Lett.* **65**, 401 (1990); W. Giele, E.W.N. Glover, and D.A. Kosower, *Phys. Rev. Lett.* **73**, 2019 (1994).

18. S. Abachi *et al.*, *Phys. Lett.* **B357**, 500 (1995).

19. B. Abbott, "The Dijet Mass Spectrum and Angular Distributions with the DØ Detector", *Proceedings of the 11th Topical Workshop on Proton–Antiproton Collider Physics*, Padova, Italy (1996), to be published.

20. V.D. Elvira, "Inclusive Jet Cross Sections at the DØ Detector", *Proceedings of the 8th Meeting, Division of Particles and Fields of the American Physical Society*, University of New Mexico, Albuquerque, New Mexico, August 2-6, 1994, p. 1637.

21. S. Abachi *et al.*, *Phys. Rev. Lett.* **75**, 618 (1995).